Framework to optimise two-dimensional DIC measurements at different orders of accuracy for concrete structures

Qifang Liu[a], Daniel Ting-Wee Looi[b], Helen Hongniao Chen[c], Chen Tang[d], Ray Kai Leung Su[e,1]

[a] *Institute of Urban Smart Transportation & Safety Maintenance, Shenzhen University, Shenzhen, China*

[b] *Faculty of Engineering, Computing and Science, Swinburne University of Technology, Sarawak, Malaysia.*

[c] *Space Structures Research Center, Guizhou University, Guiyang, China*

[d] *School of Electronic Information Engineering, University of Tianjin, Tianjin, China*

[e] *Department of Civil Engineering, The University of Hong Kong, Pokfulam Road, Hong Kong, China*

Abstract: Despite the widespread application of digital image correlation (DIC) method in concrete structures, there is no standard procedure to systematically optimising the parameters of DIC. A framework is thus proposed in this paper to optimise two-dimensional (2D) measurements with DIC at different orders of accuracy required in concrete structure models. An accuracy analysis method acting as the core of the framework is introduced and illustrated through specific case studies on reinforcement corrosion, concrete crack and seismic performance of concrete structures, as well as an example of a specific subset size. The parameters presented in the case studies and the example can act as a sound reference for selections of parameters in using DIC for concrete structures. The framework can be used as a guideline for structural engineering researchers who use DIC to measure displacement and strain at different orders of accuracy required for concrete structures.

Keywords: Digital image correlation; Reinforcement corrosion; Crack; Seismic performance; Concrete structures.

[1] *Corresponding author: klsu@hku.hk (RKL Su)*

1. Introduction

Displacement and strain of the concrete surface are key for understanding load-resistance mechanisms and failure modes through the formation of cracks. The use of conventional point-contact techniques, for example, with displacement sensors such as linear variable differential transformers (LVDTs) and strain sensors such as strain gauges (SGs), present challenges in collecting full field deformation information. This is due to the limited discrete point data that can be gathered from a single test, even though these techniques are commonly used. Alternatively, digital image correlation (DIC) technique, a non-contact optical technique, can determine the full-field surface displacement by post-processing of digital images in which the photographed surface is covered with artificial speckle patterns and then compared before and after deformation [1, 2]. Its good precision and the ability to monitor real-time full-field displacement have resulted in extensive applications of DIC in studies on the fracture behaviour [3-6], static/seismic performance [7-13] and durability [14, 15] for concrete structures.

The accuracy of DIC measurements essentially depends on the speckle pattern, image quality and input parameters for data processing [16-18]. The input parameters of processed data such as subset size (a small subsection of the reference image) and step size (the spacing between subsets) in turn depend on the speckle pattern and image quality [19]. Despite the prevalence of using DIC to examine concrete structures, minimal research has been done to detail the specification of image acquisition system and selection of parameters for data processing, except for Lin et al. [5] and Michel et al. [14]. Although the effects of subset size, size of zone of interest (ZOI) and image quality on DIC measurement have been investigated [19-23], there is no standard procedure for systematically designing image acquisition system and optimising input parameters of DIC. Consequently, it remains a challenging task to design image acquisition system and speckle pattern to attain high-quality image and select appropriate parameters for data processing, especially in examining concrete samples for different orders of accuracy.

To be specific, in some cases, displacement needs to be accurate in the order of micrometres for small-scale concrete samples [14, 15], which is a huge challenge to the image acquisition system and data processing algorithm. Although the required accuracy of displacement to be measured for large-scale or full-scale concrete structures only needs to be in the order of millimetres or centimetres [13], difficulties arise from the huge size of ZOI to be balanced with accuracy of measurement. In addition, disturbances due to vibration and fluctuation in illumination are always difficult to be eliminated in larger-scale or full-scale experiments. This will result in noises of recorded images and increase difficulties of parameter selection to attain the required accuracy. Importantly, it is usually expensive and time-consuming to conduct trial tests for long-term experiments or large and full-scale experiments. Although real images with available camera and setup are the best way to evaluate measurement accuracy, they are generally unavailable at the stage of experimental design before implementation. Hence, how to design and select the image acquisition system, speckle pattern and parameters for data processing to attain the required accuracy, may create confusions to researchers who are not familiar with DIC.

Therefore, this study intends to address the research gap to use DIC at different orders of accuracy required in concrete structure experiments and providing a framework that optimises the design of image acquisition system and parameters of DIC with an accuracy analysis. The proposed accuracy analysis method can estimate the theoretical accuracy for selection of camera, fabrication of speckles on samples and evaluation of the feasibility of experimental scheme, which is useful and worthy in designing for experiment which requires contactless full field displacement measurement. The framework can be used as a guideline for structural researchers/engineers who use DIC to measure displacement and strain across different scales of concrete structures. An example of a subset size of 45 × 45 pixels is presented with different target mean speckle size (m) and target average speckle spacing (ρ) to determine the accuracy of the DIC measurements through the mean error and standard uncertainty. The presented specification of camera and lens, as well as selected speckle size, subset size and step size of case studies can be taken as rational estimation when applying DIC for reinforcement corrosion induced concrete crack, crack measurement of pre-notched concrete beam and seismic performance of RC shear walls. This study can benefit the universal application of DIC in displacement and strain measurement for concrete structures.

2. Basic principles and parameters of DIC method

As schematically shown in Fig. 1, a reference subset of (2M+1) × (2M+1) pixels (where M is an integer as defined in Eq. (1)) centred at point $C(x_0, y_0)$ in the reference image is found in the deformation image. Prior to the matching process, a correlation criterion is predefined to evaluate the similarity between the reference and the target subsets. Once the position and shape of the target subset with the most similarities are found, the displacement vector (u, v) and the gradients from $C(x_0, y_0)$ to $C'(x'_0, y'_0)$ can be determined, where u and v are the displacements in accordance with the X- and Y-axes as shown in Fig. 1, respectively. The full-field deformation of the ZOI is obtained by repeating this correlation process with a prescribed step size for the entire ZOI [19].

As an optical method based on image matching, the accuracy of DIC relies on the correlation criteria and optimisation algorithms to correctly determine the correspondence between subsets [24]. The zero-normalised sum of squared differences (ZNSSDs) correlation criteria combined with a Newton-Raphson (NR) optimisation algorithm is widely used for detecting displacement with the DIC method due to their exceptional noise resistance and ability to correct for changes in the greyscale resultant of fluctuations in illumination [24]. The equation for the ZNSSD is expressed as [24, 25]:

$$C_{ZNSSD} = \sum_{i=-M}^{M} \sum_{j=-M}^{M} \left[\frac{f(x_i, y_j) - f_m}{\Delta f} - \frac{g(x_i', y_j') - g_m}{\Delta g} \right]^2 \tag{1}$$

where $f(x_i, y_j)$ and $g(x_i', y_j')$ are the greyscale intensity value at point $P(x_i, y_j)$ in the reference image and $Q(x_i', y_j')$ in the image of the deformation, respectively. The average greyscale intensity value of the reference image and deformation image are, f_m and g_m, respectively. Correspondingly, the standard deviation of the greyscale intensity value in the reference image and deformation image are Δf and Δg, respectively.

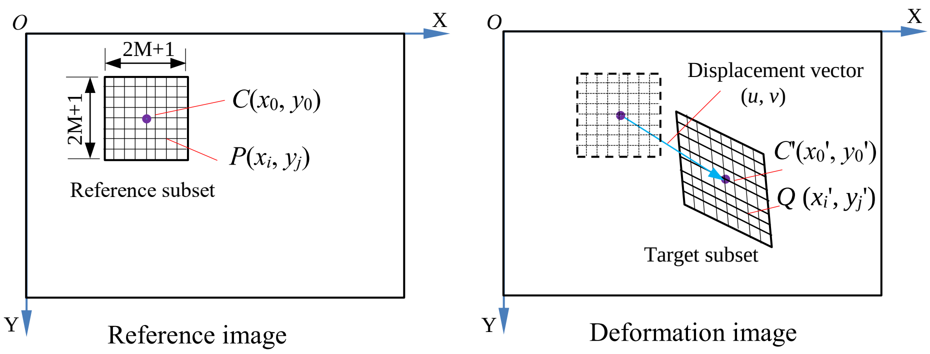

Fig. 1. Schematic of reference and target subsets in 2D DIC.

In 2D DIC method, artificial speckle pattern is commonly applied to the surface of a sample to create a distribution of random greyscale intensity [23, 25], which may influence the accuracy and precision of the DIC measurement. The production of nonperiodic and non-repetitive patterns with high contrast is among the top priorities for accurate results in DIC measurements. Hence, related parameters, i.e. speckle size and speckle spacing, should be carefully considered.

The subset shape functions (ξ and η) are always introduced to transform pixel coordinates in the reference subset into coordinates in the target subset after deformation [19], i.e.,

$$x_i' = x_i + \xi\left(x_i, y_j\right);\ y_j' = y_j + \eta\left(x_i, y_j\right);\ i, j = -M : M \tag{2}$$

By using first-order shape function, the matching algorithm is not limited to finding a pure translation, but includes other typical deformation configurations including rotation, tensile, and shear which can be extended. The first-order shape function $\xi_1\left(x_i, y_j\right)$ and $\eta_1\left(x_i, y_j\right)$ can be expressed as [26]:

$$\xi_1\left(x_i, y_j\right) = u + u_x \Delta x + u_y \Delta y \tag{3}$$

$$\eta_1\left(x_i, y_j\right) = v + v_x \Delta x + v_y \Delta y \tag{4}$$

where $\Delta x = x_i - x_0$, $\Delta y = y_j - y_0$, (u, v) is the displacement vector at the reference subset center, and u_x, u_y, v_x, v_y are the first-order displacement gradients of the reference subset in the respective x and y-axes.

As integer pixel displacement with an accuracy of one pixel can be readily computed for digital images, a sub-pixel registration algorithm [24, 27] can actually be the key for improving displacement measurements to a sub-pixel accuracy in the DIC method. The one-pixel accuracy has been determined by the image acquisition system, whist the sub-pixel accuracy is highly dependent on the speckle size, speckle spacing, subset size and step size [21, 28].

3. Framework on optimisation of 2D DIC measurements

A flowchart that shows the process for optimising 2D DIC measurements for concrete structures at different scales and order of accuracy is presented in Fig. 2. The procedures are briefly described as follows:

(1) Determination of order of displacement approximation to be measured

The accuracy of the displacement is required at different orders for small-scale, large-scale and full-scale concrete structures. Estimating the displacement is the crucial first step in optimising 2D DIC displacement measurements.

(2) Selection of appropriate cameras

Based on the estimated order of displacement and the area of the ZOI, the required spatial resolution of the recorded images can be preliminarily determined by considering a displacement to the accuracy of one-pixel. To reduce the noise in the image, high performance cameras are recommended.

(3) Selection of DIC parameters

There are two types of parameters that need to be selected: (i) image related parameters and (ii) algorithm related parameters. The former includes speckle size and speckle spacing. Algorithm related parameters mainly consist of subset size and step size. To obtain the full field displacement, the step size should not exceed half of the subset size. As speckle patterns are randomly produced on the surface of the sample, the speckle distribution is quantified by the average spacing ρ of the speckles as:

$$\rho = \sqrt{N^2/S} \tag{5}$$

where S is the total number of speckles in a defined area of $N \times N$ pixels.

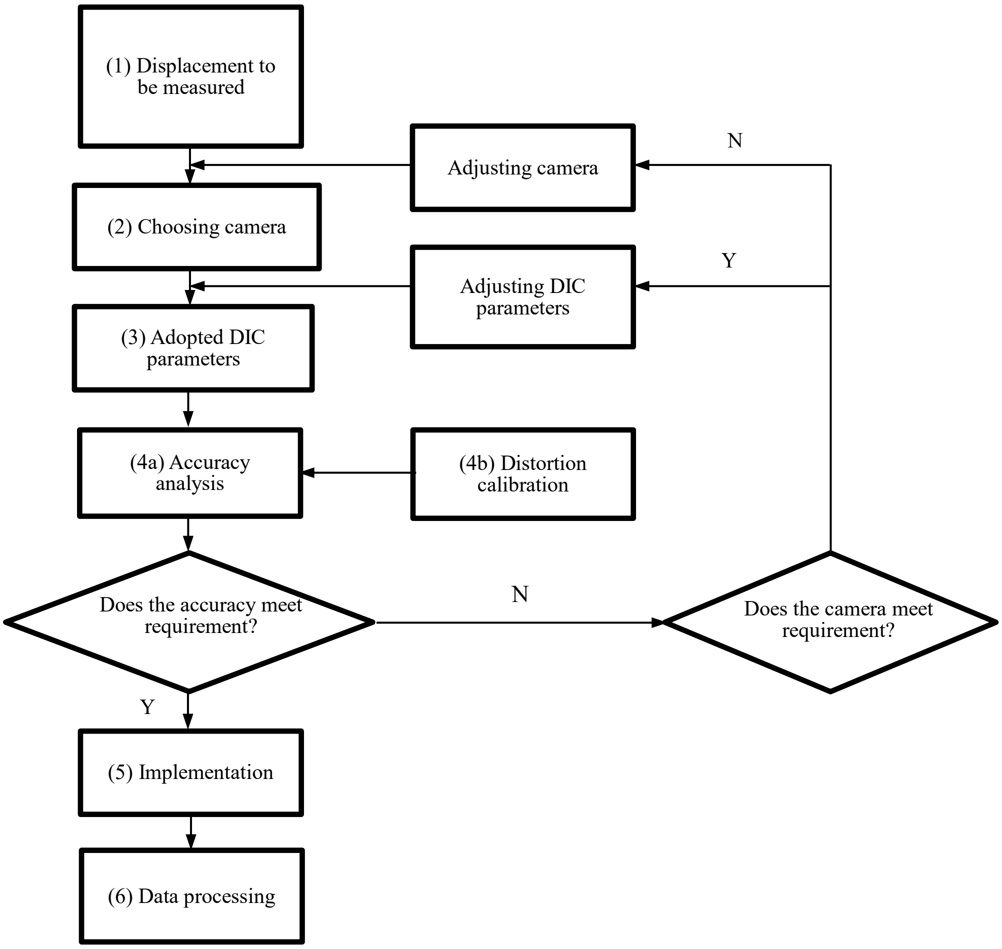

Fig. 2. Flowchart: Optimising displacement measurement with 2D DIC.

(4a) Implementation of accuracy analysis

An accuracy analysis can be carried out using one of two methods depending on the scale of displacement. Method (A) is an a priori analysis procedure, which is generally applicable for any scale of displacement but exceptionally useful for measurements in concrete structures targeted at micrometre scale. This is simply because there are no commonly available point-contact measurement devices (i.e. LVDTs and SGs) which have reliable enough sensitivity to measure the scale of displacement in the order of micrometres. Method (B) is a rational procedure for a scale beyond the order of millimetres, which can be adequately calibrated by LVDTs and SGs.

Method (A):

A priori analysis which uses simulated speckle images is proposed to estimate the accuracy of measured displacement with the selected parameters. The simulated images before and after deformation are produced with the method proposed by Zhou and Goodson [28], assuming that the speckle patterns before and after deformation $I_1(\mathrm{r})$ and $I_2(\mathrm{r})$ are the sum of the individual speckles approximated by a Gaussian function:

$$I_1(\mathbf{r}) = \sum_{k=1}^{S} I_0 \exp\left(-\frac{|\mathbf{r}\text{-}\mathbf{r}_k|^2}{m^2} \right) \tag{6}$$

$$I_2(\mathbf{r}) = \sum_{k=1}^{S} I_0 \exp\left(-\frac{|\mathbf{r}\text{-}\mathbf{U}(\mathbf{r})\text{-}\mathbf{r}_k|^2}{m^2} \right) \tag{7}$$

where I_0 is the peak intensity of each speckle, m is the speckle size, and $\mathbf{r}_k = (x_k, y_k)^T$ is the randomly distributed position of each speckle. The displacement $\mathbf{U}(\mathbf{r})$ is defined as:

$$\mathbf{U}(\mathbf{r}) = (u_0 + u_x x + u_y y, v_0 + v_x x + v_y y)^T \tag{8}$$

where $\mathbf{U}_0 = (u_0, v_0)^T$ is the displacement at $\mathbf{r} = (x, y)^T$, and $\nabla \mathbf{U}_0 = \begin{pmatrix} u_x & u_y \\ v_x & v_y \end{pmatrix}$ is the deformation gradient.

Three typical deformation configurations can be conveniently used to generate speckle image pairs before and after deformation, i.e., (a) rigid body translation with $\mathbf{U}(\mathbf{r}) = (u_0, 0)^T$, (b) rigid body rotation with $\mathbf{U}(\mathbf{r}) = (\varepsilon \cdot y, -\varepsilon \cdot x)^T$ and (c) uniaxial tensile with $\mathbf{U}(\mathbf{r}) = (\varepsilon \cdot x, 0)^T$, where ε is a nonnegative value.

The measurement accuracy of DIC can be validated by comparing the processed results with the preassigned deformation. It is virtually impossible to obtain the desired accuracy with the selected parameters with a single step. Hence, Steps 2 to 4 need to be iterated to reach a set of optimal parameters.

Method (B):

This method does not require artificial preassigned image deformations. The accuracy analysis can be simply carried out by comparing the DIC results with those carried out by a point-contact measurement device such as an LVDT or SG. However, the drawback of this method requires the generation of speckle patterns on a real concrete sample subjected to deformation, which can be uneconomical and time consuming.

(4b) Camera lens calibration

When carrying out DIC measurements, distortion from the camera lens needs to be corrected. Given that the potential of lens distortion may create substantial measurement errors (deviation of several pixels) when using the pinhole model to predict image location, it is essential to remove distortions from image-based measurements [24]. The most widespread approach to circumvent distortion is to use the parametric distortion model by adding a distortion vector term to the pinhole prediction model. Alternative approaches are, for example, the planar target grid approach and the a priori distortion model. Details on image calibration and distortion correction can be found in [24].

(5) Implementing DIC

After selecting the appropriate parameters, measurement can be carried out through DIC, with preparation of speckled samples, image acquisition and image analysis.

(6) Processing data

By conducting post-processing analysis such as displacement smoothing and strain de-noising, displacement and strain can be extracted from the acquired images.

The proposed framework and a priori analysis method provide guidelines on setting up the system for speckle pattern production and image acquisition, including estimating measurement accuracy. The framework has substantial significance when experimental testing is costly and time consuming.

4. Case study of RC structures

Three case studies are presented in this paper to show the necessity of optimising the input parameters and the application of the proposed framework towards different orders of measurement accuracy required in concrete structures. It is noted that the selection and setup of the image acquisition system in the case studies (Step 2 of the framework) and the optimisation of DIC parameters (Step 3 of the framework), were not determined with one single step but through trial and error by conducting accuracy analysis (Step 4a of the framework), in which lens distortion was corrected (Step 4b of the framework). To present the application procedures of the framework in a concise way, the iterative process from Steps 2 to 4 is disregarded. Nonetheless, the necessity to optimise DIC measurement and the selected camera and parameters will be discussed for each case study.

4.1. Introduction of the adopted camera and DIC software

Digital single-lens reflex (DSLR) camera was adopted in the case studies for the following reasons: (i) The monochrome camera is preferred over the DSLR camera of the same resolution because the light intensity of each pixel is accurately registered [29]. However, the price of a monochrome camera is too much more expensive than that of a DSLR camera, which is always the limitation of its practical application. (ii) The DSLR camera uses a colour filter array (CFA) to separate colour channels. As a result, the colour information must be converted into a monochrome signal by using demosaicing algorithms which may have effects on eventual result. The single integer bias of DSLR camera is of the same order of magnitude as that of monochrome camera, whereas bi-integer bias was observed in the DSLR camera but not in the monochrome camera which may cause a larger error of DIC results [29]. However, with additional resolution, the more affordable DSLR camera appears to be attractive for long term testing and crack detection as demonstrated in the case studies in this paper [14, 30, 31], provided that the user has good understanding of performance and accuracy feature of DSLR camera.

A DIC software, Optecal [32], which is programmed based on the Levenberg-Marquardt (LM) subpixel registration technique [24] and ZNSSD correlation criterion, was applied in the case studies. Fig. 3 shows an example of the deformation contours of the three case studies of concrete structure, which were produced using Optecal. Optecal enables lens distortion calibration by using a built-in database of lens distortion parameters to correct the RAW images. Alternatively, engineers can also make use of Hugin software [33] and an open source Camera Calibration Toolbox for MATLAB [34], to calibrate camera lens and input the parameters in Optecal for distortion correction. The comparison between displacement calibrated by the two approaches show a difference of about 0.05 pixel. In this paper, the Camera Calibration Toolbox for MATLAB was utilised for case study 1, whist the Hugin software was adopted for case studies 2 and 3. The calibration process of Camera Calibration Toolbox for MATLAB is automated which may reduce the error of manual selection when using Hugin software. However, the Toolbox for MATLAB needs dozens of input images of a standard checkerboard captured at different directions with fixed focal length, focus position and aperture (see Fig. 4a), whist only one picture with captured man-made line is necessary in Hugin software for given focal length, focus position and aperture (see Fig. 4b). Readers can choose one of the methods for their convenience. It is noted that various DIC software calibrates lens distortion with different approaches. Since the proposed DIC framework in this paper is generic, readers have the option to choose any other DIC software. Nonetheless, it is recommended to compare the results of different

DIC software for verification purposes.

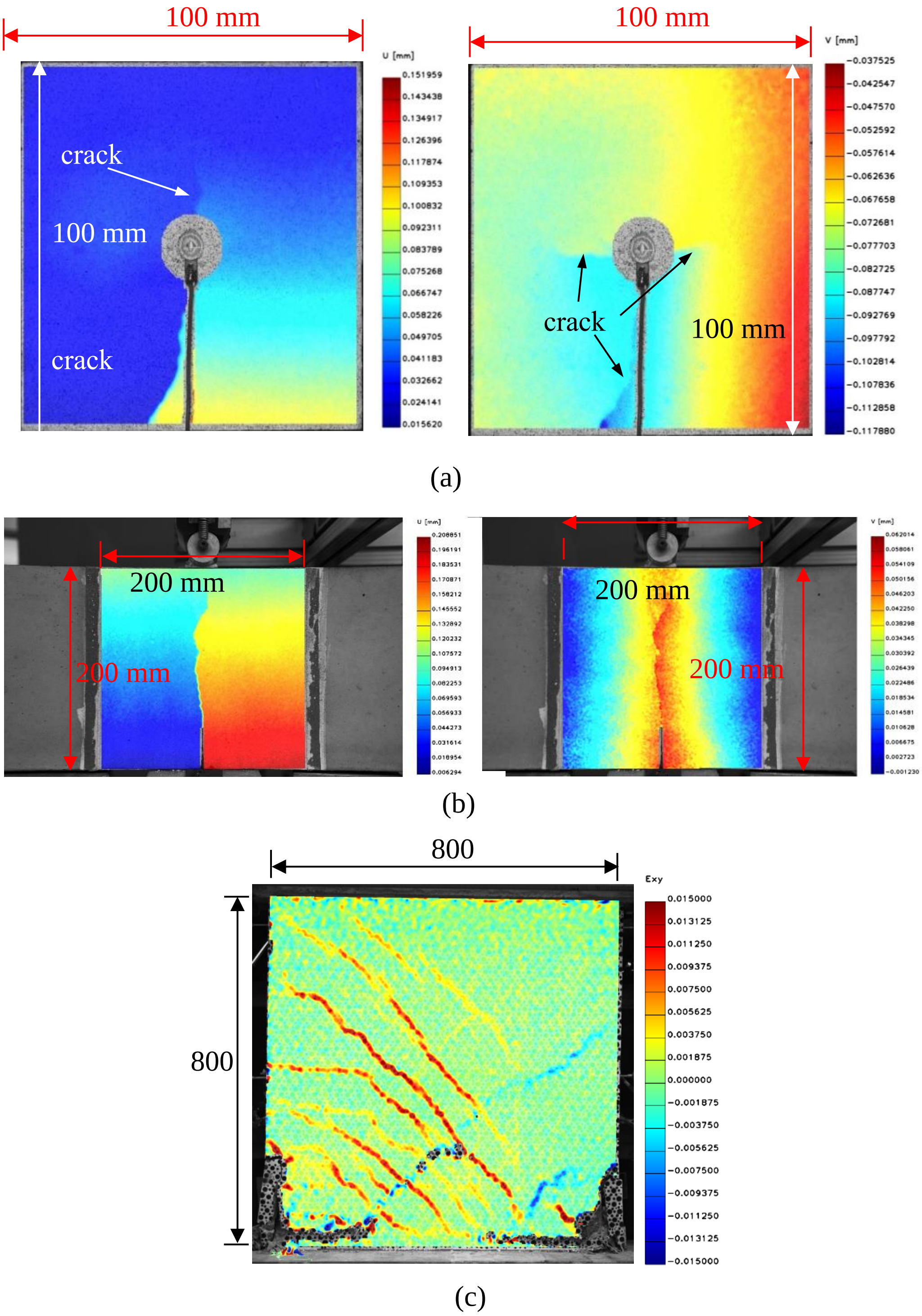

Fig. 3. Deformation or strain contours from DIC analysis for three case studies at different orders of scales: (a) crack from accelerated corrosion in concrete test (b) pre-notched concrete beam test (c) cyclic RC shear wall test (shear strain).

(a) (b)

Fig. 4. Lens distortion calibration methods: (a) Image of a standard checkerboard captured at different directions for the Camera Calibration Toolbox in MATLAB and (b) Input image of man-made lines utilised in Hugin software.

4.2. Case Study 1: Crack measurement of reinforced concrete in accelerated corrosion test – displacement accuracy at micrometre (μm) scale.

Due to the convenience and effectiveness of measuring displacement over a long period of time, the DIC technique has been used in the study of reinforcement corrosion in concrete [15]. A setup for steel corrosion induced cracks in reinforced concrete (RC) is shown in Fig. 5. The concrete sample was a 100 mm × 100 mm × 50 mm block with a rebar cast in the centre. The ultimate compressive strength of the concrete was 67 MPa, and the rebar diameter was 12 mm. The accelerated corrosion process was achieved by submerging the concrete block into a sodium chloride (NaCl) solution and applying a constant current.

Due to the volume expansion of corrosion products of steel, expansive pressure is produced at the concrete/steel interface and induces deformation and cracks of the surrounding concrete [35]. The surface displacement is monitored by using DIC, with the aim to determine the critical threshold for displacement due to expansion when cracks develop at the surface cover of the concrete.

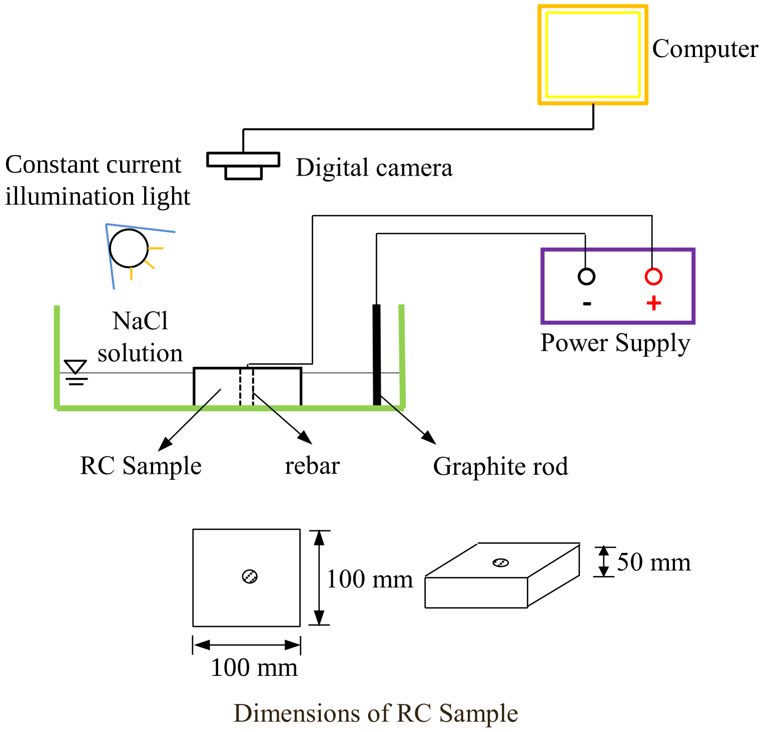

Fig. 5. Schematic setup of displacement measurement with 2D DIC for reinforcement corrosion in concrete.

The critical threshold for displacement due to expansion can be approximated with a smeared crack model [15], which is found to be about 12.5 μm. This is indicated as the first step of the proposed framework. As shown in Fig. 5, a digital camera (Canon EOS-80D) with 24 megapixels (6000 × 4000 pixels) was placed directly over the sample. The captured images were saved as Canon RAW CR2 format. The camera lens used was a Canon EF-S 18-55 mm f/3.5-5.6 IS STM lens. The desired full field image of the sample was acquired by applying a maximum focal length of 55 mm with the lens placed at 32 cm away from the sample. The resultant scale is one pixel equals to 25 μm. Two LED lights powered by a constant current were installed to reduce the fluctuations from illumination lighting. As the integer pixel accuracy can only reach a maximum of 25 μm, it is necessary to optimise the parameters based on an a priori accuracy analysis to achieve higher sub-pixel accuracy.

4.2.1. Subset size and step size

To select the optimal subset size and step size, simulated images before and after deformation were produced with the method proposed in Eqs. (6)-(8). To simulate the image noise from the environment and the camera itself, a random noise with a signal-to-noise ratio (SNR) of 20 dB [36] for acceptable image quality was added. The average speckle spacing in an image of 500 × 500 pixels was set as $\rho = 10$ pixels. The speckle size was m = 5 pixels. The preassigned rigid displacement and uniaxial tensile strain were 0.1 pixel and 1000 με, respectively. As the applicability of the measurement results is determined by their uncertainty component [37], the mean error and standard uncertainty [19, 21] which characterise the bias and precision of the measured displacement and strain were analysed, and the results are shown in Figs. 6 and 7. The standard uncertainty can be accounted by the standard deviation (STD), σ [37]:

$$\sigma = \sqrt{\frac{1}{n-1}\sum\left(\chi - \bar{\chi}\right)^2} \tag{9}$$

with

$$\bar{\chi} = \frac{1}{n}\sum\chi \tag{10}$$

where n is the number of observations, and χ is the observed value of the measurand.

Fig. 6 shows the effect of the subset size on the measurements. The step size is set to be 0.375 times that of the subset size (see discussion in Fig. 7). The increasing subset size as shown in Fig. 6(a) implies that the mean displacement error slightly increases; however, the standard uncertainty of the displacement initially decreases followed by a slight increase. When the subset size is less than or equal to 45 × 45 pixels, the increasing subset size can significantly reduce the standard uncertainty of strain, as shown in Fig. 6(b), but has a negligible effect on the mean strain error. This is similar to the observations reported by Pan et al. [19] and Sun and Pang [38]. The highest standard uncertainties of displacement and strain were recorded when the subset size is

21 × 21 pixels. The optimal subset size is thus 45 × 45 pixels.

Fig. 7(a) shows that the mean error and standard uncertainty of displacement in a pixel unit span across the step size. The graph shows an initial increase, followed by decrease with step size increments. The mean error and standard uncertainty of displacement peak at a step size of 0.25 times the subset size. In Fig. 7(b), the mean error and standard uncertainty of strain in general show an increase with step size increments. The minimum mean error and standard uncertainty of strain are consistently achieved when the minimum step size (the spacing between the subsets, taken as 0.1 times the subset size) is selected. In contrast, both the mean strain error and standard strain uncertainty reach their maximum at the maximum step size (which is 0.5 times the subset size). This is because increasing the step size reduces the number of calculated points, which results in a larger mean error and greater uncertainty of strain. It should be noted that the number of calculated points and computational time increase with a smaller step size. An appropriate step size that is 0.375 times the subset size (which is less than half of the subset size and equals to 16 pixels in this case) is selected by considering both accuracy and the computational cost of calculation.

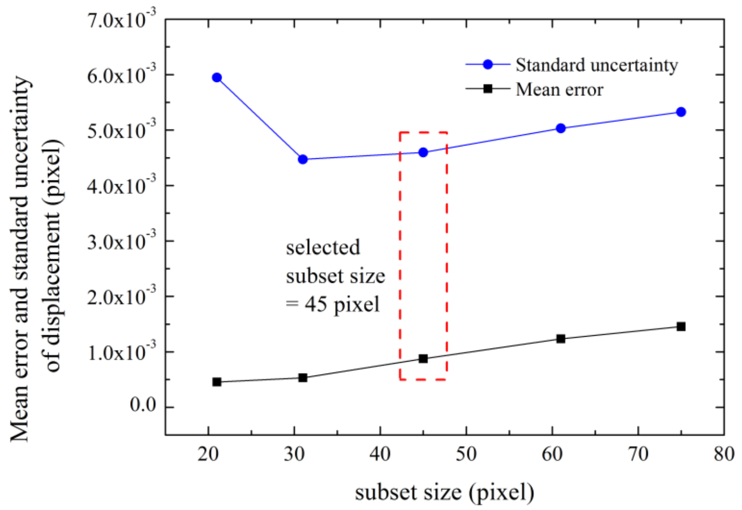

(a)

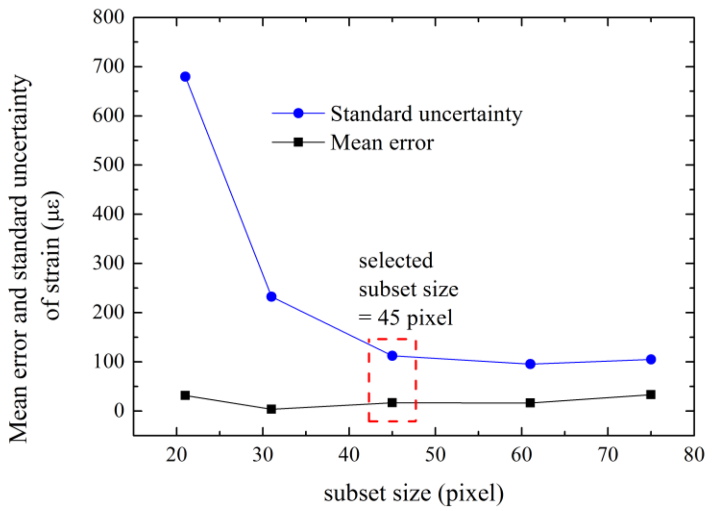

(b)

Fig. 6. Mean error and standard uncertainty of (a) displacement and (b) strain variations with different subset size. (Note: Step size: 0.375 times subset size.)

351

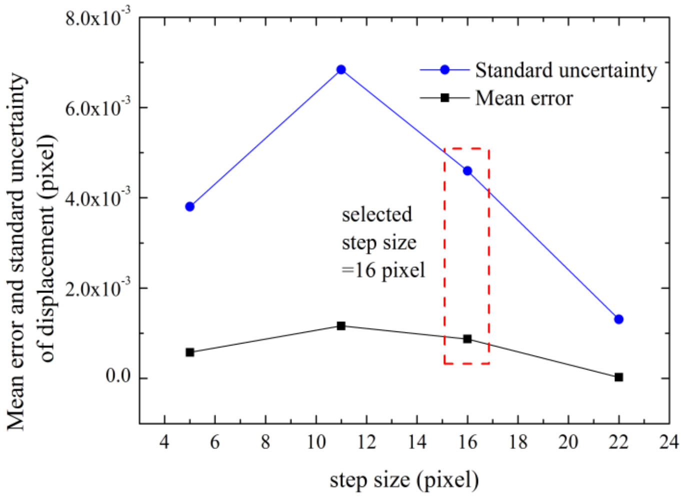

(a)

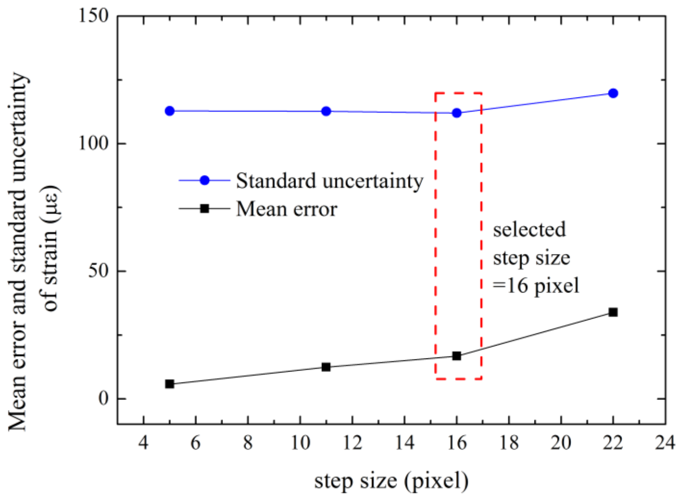

(b)

Fig. 7. Mean error and standard uncertainty of (a) displacement and (b) strain variations with different step size (0.1, 0.25, 0.375, and 0.5 times subset size). (Note: Subset size set at 45 × 45 pixels.)

4.2.2. Speckle size and spacing

A similar procedure as that for determining the optimal subset size and step size was conducted for mean speckle size *m* and average speckle spacing ρ, to investigate their effects on measurement accuracy and precision. A subset size of 45 × 45 pixels and step size of 16 pixels (which is 0.375 times the 45 pixels) were applied based on the findings in previous section. The rigid displacement and uniaxial tensile strain were preassigned as 0.1 pixel and 1000 με, respectively. The results are shown in Table 1. It can be observed that reducing the speckle size or speckle spacing does not guarantee a lower mean error and standard uncertainty of the displacement and strain. However, the mean displacement and strain error, and the standard uncertainty of strain generally decrease when the speckle size is reduced (i.e., when $1 \le \rho/m \le 3$). The mean displacement and strain error of m = 15 pixels are much larger than that of m = 10, 5 pixels.

Table 1 Mean error and standard uncertainty of displacement and strain for different spacing ρ and speckle size m with subset size = 45 × 45 pixels, and step size = 16 pixel.

ρ (pixel)	m (pixel)	Mean error of displacement (pixel)	STD of displacement (pixel)	Mean error of strain (με)	STD of strain (με)
15	15	2.46×10^{-3}	8.82×10^{-3}	104.59	588.09
20	15	2.87×10^{-3}	8.06×10^{-3}	52.08	390.48
10	10	9.79×10^{-4}	6.48×10^{-3}	14.30	234.11
15	10	1.93×10^{-3}	6.43×10^{-3}	9.97	215.91
20	10	7.14×10^{-4}	5.44×10^{-3}	1.35	251.42
5	5	7.80×10^{-4}	5.13×10^{-3}	16.76	129.68
10	5	8.73×10^{-4}	4.60×10^{-3}	16.73	112.03
15	5	7.13×10^{-4}	4.58×10^{-3}	15.65	160.56
20	5	7.89×10^{-4}	7.11×10^{-3}	2.36	602.56

In addition, for the same speckle size (m = 5), smaller spacing ρ (i.e. higher speckle density) does not necessarily improve accuracy and precision. As shown in Table 1, the mean error and standard uncertainty of the displacement and strain for ρ = 5, 10, 15 and 20 have insignificant differences. However, when $\rho/m \ge 3$, i.e. ρ = 20, the standard uncertainty of strain drastically increases while the mean error of strain is reduced. The speckle images with different speckle spacing in Fig. 8 show that when ρ / m = 2~3, the images have the best contrast performance. It should be noted that in practice, the generated speckles may not be easily nor perfectly controlled so that they are of the same size. Therefore, a range of speckle size of m = 3~8 pixels and ρ = 10~15 pixels were selected to produce averaging effects in the reinforcement corrosion experiment. The surface of the concrete sample with artificially generated speckles is shown in Fig.

9.

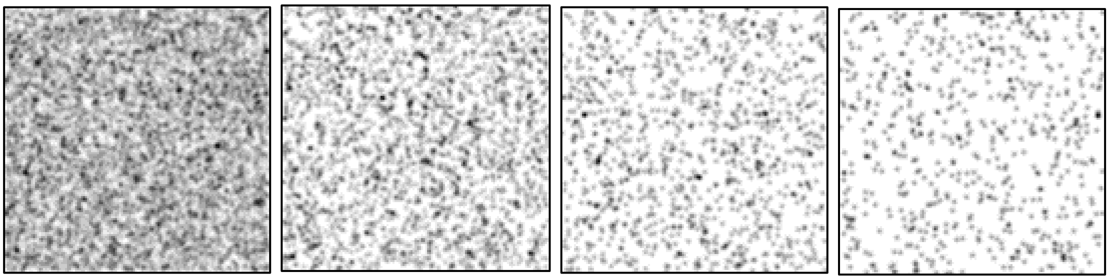

(a) ρ = 5 pixels (b) ρ = 10 pixels (c) ρ = 15 pixels (d) ρ = 20 pixels

Fig. 8. Images of speckles with different densities.

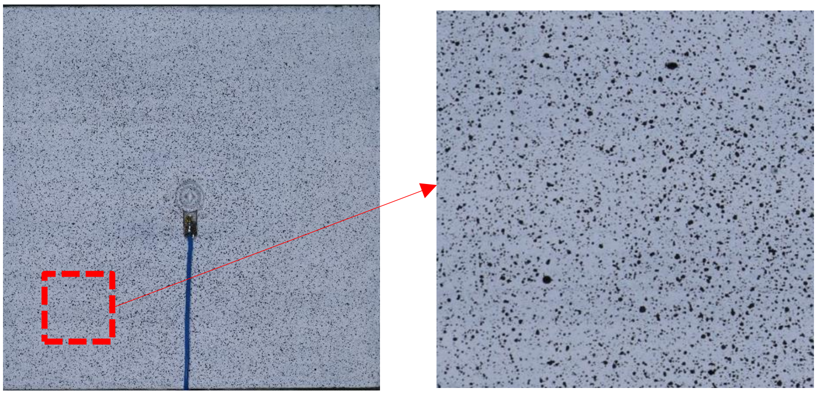

(a) (b)

Fig. 9. Concrete sample with artificially generated speckles. (a) On sample surface. (b) Enlarged sub-region of sample surface: 500 × 500 pixels.

4.2.3. Measurand

Very often, LVDTs or SGs cannot be used for smaller concrete samples in which the accuracy of the displacement value is at the micrometre scale. The performance of DIC with the selected parameters that measure different scales of measurands is evaluated. Fig. 10 shows the STD of each mean observation of the DIC for different preassigned rigid body translations and uniaxial tensile strains. As shown in Fig. 10, the mean observation of the measurand is accurately captured, while the precision increases with increases in the preassigned deformation.

Fig. 10(a) shows rigid body translations greater than 0.05 pixel can be captured accurately and precisely. When the preassigned rigid body translation is 0.01 pixel, the STD of the mean observation of 0.0097 pixel is 1×10^{-3} pixel. Therefore, with a scale of 1 mm = 40 pixels, displacement over 1.25 μm can be accurately and precisely measured. Fig. 10(b) shows that the STD of tensile strain greater than 300 με is 43 με (coefficient of variation = 0.14). However, the STD of strain less than 100 με is at most 35 με (coefficient of variation = 0.35), which means that it is difficult to precisely capture strain in the order of less than 100 με.

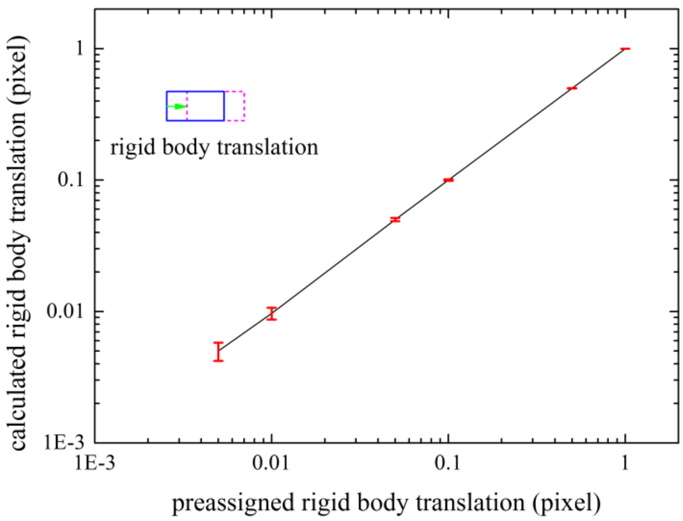

(a)

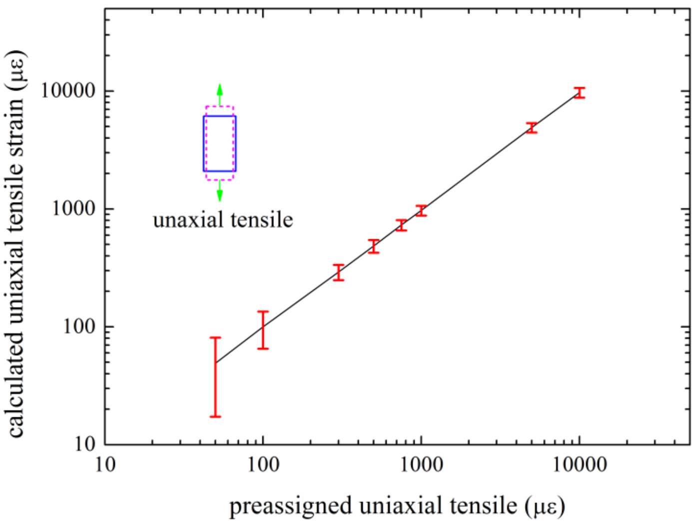

(b)

Fig. 10. Validation of accuracy of DIC algorithm under (a) rigid body translation and (b) uniaxial tensile.

It is noted that the simulated image analysis is presented as a theoretical approximation of the real levels of accuracy, which is useful and more convenient when checking feasibility of experimental scheme. However, real images produced by moving the specimen or camera using a micrometer stage will be complementary to accuracy analysis with simulated images, which is worthy to be extended in future work.

4.3. Case Study 2: Crack measurement of pre-notched concrete beam for non-linear fracture mechanics study – displacement accuracy at micrometre (μm) to millimetre (mm)

Non-contact optical techniques are effective means to investigate nonlinear fracture behaviour of quasi-brittle materials, e.g. concrete, due to their capacity to accurately record crack development and full-field displacement in the fracture process zone (FPZ), which is shown in Fig. 11. Electronic speckle pattern interferometry (ESPI) is a non-destructive optical technique which enables measurement of surface displacement by analyzing the variation of fringe pattern. Chen and Su [39] demonstrated the use of ESPI to evaluate crack characteristics including complete crack opening displacement (COD) profiles, width of the FPZ and crack length. The results were used to estimate the tension-softening of concrete. Although DIC is similar to ESPI, it is however relatively simpler and more convenient in terms of experimental setup and data processing. Both methods have high level of accuracy that can be achieved with less strain sensitivity on vibration. Therefore, DIC is a good alternative for investigating the nonlinear fracture behaviour of concrete.

As shown in Fig. 11, a three-point bending test of a pre-notched beam is conducted to investigate the fracture mechanical properties of concrete in accordance with RILEM recommendations [40]. The ultimate compressive strength of the pre-notched concrete beam is 65.1 MPa. The beam size is 900 mm × 200 mm × 50 mm, and the span is 800 mm. The notch length is 60 mm, and the width of the notch is 2 mm. LVDTs and clip gauge were installed at the bottom surface (soffit) of the concrete beam. The mid-span deflection and crack mouth opening displacement (CMOD) were measured by LVDTs and a clip gauge, respectively. CMOD is essential for demonstrating the nonlinear fracture behaviour of concrete. By using a very stiff servo-controlled MTS testing machine to carry out the three-point bending tests, the growth of the primary crack was well controlled. The displacement-controlled loading rate was set at 0.01 mm/min. The complete load-deflection and load-CMOD curves were recorded by using a data logger.

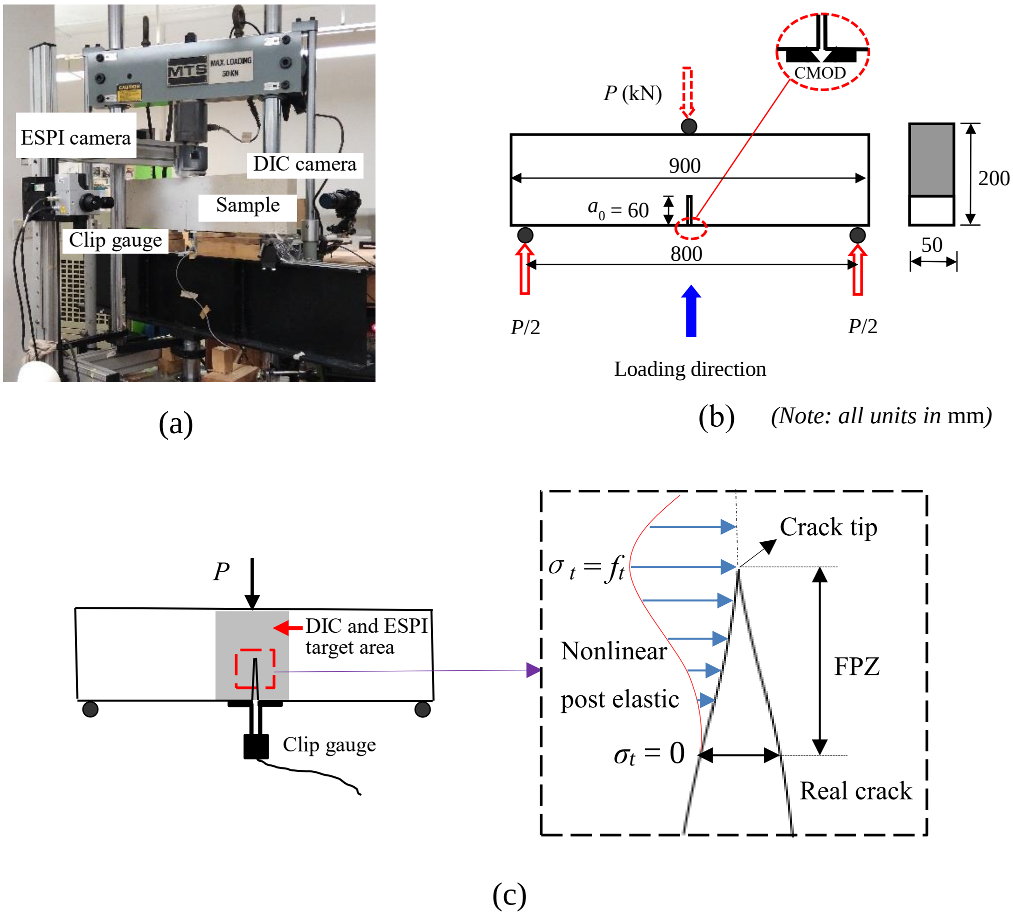

Fig. 11. Measurement of cracking in pre-notched concrete beam. (a) Experimental setup (b) Diagram of three-point bending test and (c) Sketch of FPZ (where σ_t is the tensile strength of concrete).

As the first step to optimise DIC measurement (see Fig. 2), the order of CMOD to be measured should be approximated. The critical value of the CMOD at peak load is about 70 μm, whist the CMOD is expected to be as large as 1 mm or more at the end of post-peak stage. Measurement accuracy realistically should meet this requirement at the crack tip, which should be in the order of micrometres to millimetres.

Secondly, appropriate camera for image acquisition should be selected. For comparison purposes, the progression and displacement of the cracks in the concrete beam were recorded by using both ESPI and DIC. The ESPI system (Dantec-Ettemeyer Q300) and a digital camera for DIC analysis were placed in front and at the back of the sample, respectively. The target areas for ESPI and DIC observation is the shaded areas on the front and back surface of concrete beam as displayed in Fig.11(c), respectively. The CMOD results of ESPI and DIC were evaluated at the end of the notch near to the bottom surface of the concrete beam, in order to compare with the clip gauge results. The camera of the ESPI was placed at about 430 mm away from the concrete beam. The technical specifications of the Dantec-Ettemeyer Q300 system can be found in [41]. For the DIC measurement, a Nikon D7100 camera with sensor of 24 megapixels (i.e. image size of 6000 × 4000 pixels) was adopted. The captured image format is NEF. The camera lens (AF-S DX NIKKOR 18-300 mm f/3.5-6.3G ED VR lens) with a focal length of 50 mm was placed at 1100 mm from the sample surface, which was calibrated by using Hugin software for distortion correction. The obtained lens calibration parameters were input in Optecal software to convert the captured NEF images for data processing. The scale of the measurement in the ZOI area of 200 mm × 200 mm is about 19 pixels/mm (1-pixel accuracy ≈ 0.05 mm). As a result, it becomes necessary to optimise the DIC parameters (Step 3 in Fig. 2) for good sub-pixel accuracy. The accuracy analysis (Step 4a) proposed in the framework was then carried out. As previously mentioned, it is important to note that the selection of camera or DIC parameters is not determined with a single step. Steps 2 to 4a were iterated to reach a set of optimal parameters by conducting accuracy analysis, in which the distortion was calibrated and corrected (Step 4b). Through trial-and-error, the speckle size and spacing were determined as m = 2~6 pixels, and ρ = 5~10 pixels, respectively. A subset size of 31 pixels and step size of 15 pixels were adopted.

By implementing DIC measurement (Step 5) and processing the acquired data (Step 6), the deviation between the load-CMOD measured by DIC with that measured by ESPI and the clip gauge can be evaluated. (see Fig. 12(a)). It can be observed that the load-CMOD measured by using DIC is generally consistent with that measured by the clip gauge for the entire loading period. The results demonstrated the reliability of DIC in capturing crack opening displacement. On the contrary, the load-CMOD measured by ESPI deviates from that by the clip gauge and DIC when the CMOD is greater than 0.25 mm. As shown in Fig. 12, the maximum CMOD is recorded at 1 mm. When crack propagated close to the top of the beam with increasing of CMOD (larger than 0.25 mm), it is expected that rigid rotation occurs with the sink of midspan because the bearing capacity of concrete beam decreases. This may cause severe decorrelation in ESPI laser speckle patterns [25, 42, 43] and thus produce deviation compared to clip gauge and DIC. As opposed to ESPI, most DIC algorithms have the option of retrieving displacement with the frame-compared-with-preceding-frame approach (besides the standard option of referencing the initial image), which enables DIC performs better when decorrelation occurs between the current frame and reference frame. The frame-compared-with-preceding-frame approach was adopted only at later stages of crack propagation when the CMOD is larger than 0.25 mm. Prior to 0.25 mm, the standard option of referencing the initial image was adopted.

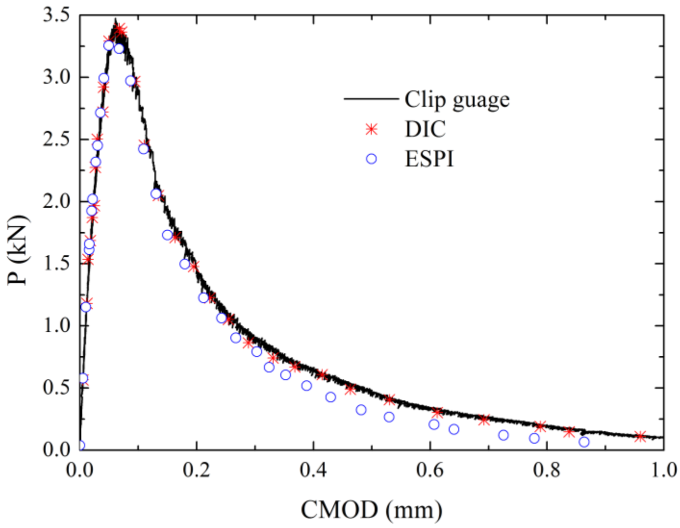

(a)

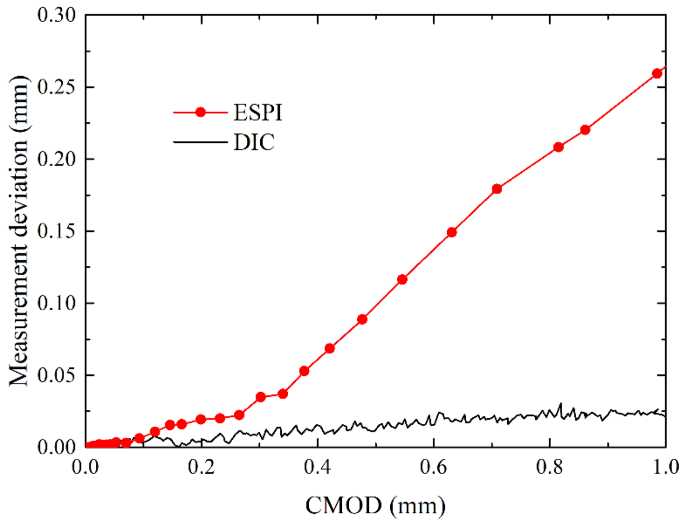

(b)

Fig. 12. Pre-notched concrete beam test results: (a) load-CMOD results from different measurement methods, and (b) measurement deviation of DIC and ESPI compared to that of clip gauge.

It is noted that when the CMOD is small (less than 0.25 mm), the measurement deviation of the DIC is less than 6 μm (see Fig. 12(b)). This may be caused by the minor difference between the evaluated location of CMOD by using DIC and clip gauge. The captured full-field displacement by DIC was on the back surface of concrete beam, whist the clip gauge was installed at the bottom surface of concrete beam where is closer to the front surface.

4.4. Case Study 3: Full displacement field measurement of RC shear walls – displacement accuracy at millimetre (mm) to centimetre (cm)

A series of RC shear wall tests were conducted in Looi et al. [13] to investigate the structural behaviour of RC walls with short shear span (a special class of RC shear walls that are found in many low-to-moderate seismic regions) under constant vertical load and cyclic lateral loading. Fig. 13(a) shows the setup of the RC shear wall test. The shear wall has dimensions of 800 mm × 800 mm × 80 mm (height × length × thickness), cast with concrete of about 30 MPa cube strength and loaded with three servo-controlled MTS actuators. DIC was used on the front face of the wall to capture the full deformation field. In this study, the lateral displacement profile of a shear wall, codenamed C30-N-ALR01 and measured by LVDT-2 and LVDT-5 will be referenced, to corroborate with the processed data of the DIC results (i.e., DIC-L and DIC-R) from a previous study [13]. It should be noted that the LVDTs were placed above the rigid RC base of the walls to automatically eliminate unwanted base sliding between the sample and the rigid platform (the frame that supports the LVDT stand is shown in Fig. 13(b).

The maximum lateral displacement is ± 10 mm. As the first step in the proposed framework (see Fig. 2), the displacement to be measured is in the order of millimetre. The second step to select the appropriate camera for image acquisition and third step to optimise DIC parameters were implemented through trial-and-error by conducting accuracy analysis (Step 4a of the framework). The selected digital camera for the DIC analysis (Canon EOS 70D with a 20.2-megapixel sensor, installed with a Canon EF-S 18-55 mm IS STM lens) was used to capture the images of the random speckles in Canon RAW CR2 format at 6-10 s intervals throughout the experiment. The ISO was set at 400 with an aperture of f/4. The camera was placed in front of the test rig at about

2 m away from the walls with the focal length of the camera lens set at 24 mm, thus allowing a ratio of about 2 pixels/mm (1-pixel accuracy ≈ 0.5 mm). When conducting accuracy analysis, post-processing of Canon RAW CR2 conversion and lens distortion (Step 4b of the framework) were carried out using the built-in function of Optecal [32] and distortion correction parameters calibrated by Hugin software [33].

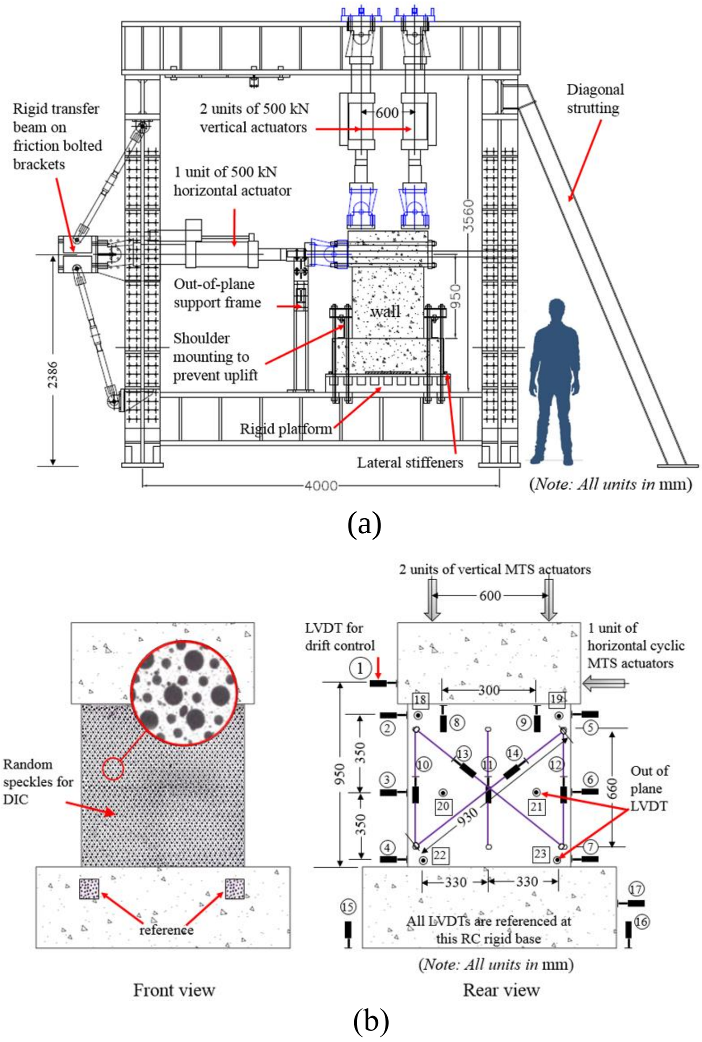

Fig. 13. RC shear wall test under cyclic loading: (a) experimental setup in testing rig (b) DIC and LVDTs.

The speckle size *m* was determined as 2~20 pixels with a mean value of about 10 pixels. Black speckles were randomly sprayed onto the walls with the use of a stencil board. The surface of the wall was coated with a thin layer of white plaster to enhance the contrasting. Random speckles were generated with diameter sizes of 1, 2.5, 5 and

10 mm and spacing at approximately 2.5 times the speckle diameter (ρ = 5~50 pixels, average spacing at about 25 pixels). The subset size of 45 x 45 pixels and step size of 13 pixels were used.

By using the selected camera and optimised DIC parameters, displacement measurement was implemented and evaluated as described in Steps 5 and 6 of the framework. Fig. 14 shows the envelope of the hysteresis loop generated by using the results of LVDT-2 and LVDT-5 at a height of 720 mm from the concrete base. Two points determined by DIC (i.e. DIC-L and DIC-R) which were measured at the same height with LVDT-2 and LVDT-5, respectively, were computed and superimposed; see Fig. 14.

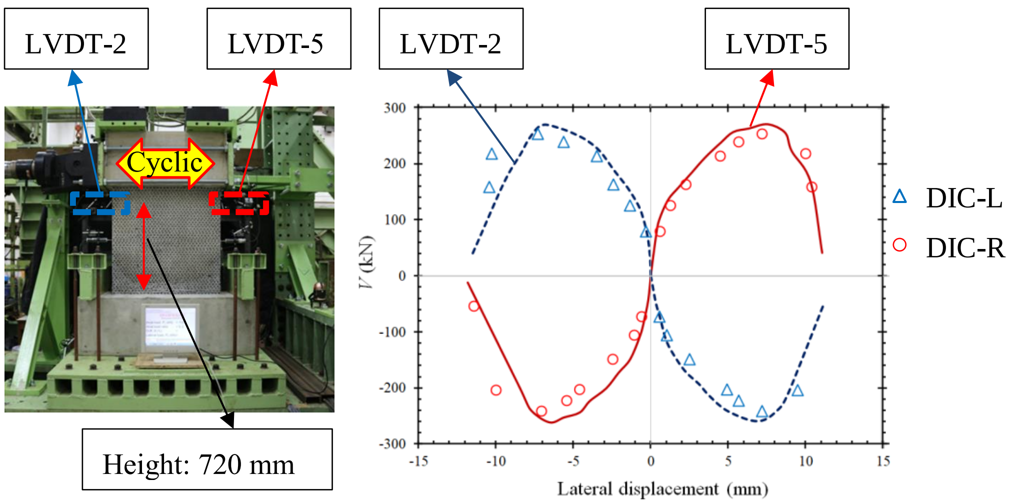

Fig. 14. Hysteresis envelope of lateral load-displacement recorded by LVDTs and DIC in RC shear wall tests under cyclic loading (Note: DIC-L compared to LVDT-2 and DIC-R compared to LVDT-5).

Fig. 15 shows the computed measurement deviation of DIC with the LVDT result. The deviation is small during the initial cyclic displacement, but increased to maximum of 1.6 mm at a displacement of 5 mm. The mean deviation is about 0.78 mm throughout the whole experiment. The maximum displacement at collapse failure in this study is recorded at about 12 mm, thus standard deviation and variation of ±1 mm are computed.

The deviations could be due to the following possible reasons: (i) minor spalling of concrete cover due to cracks, which resulted in movement of the speckles and (ii) the large scale RC wall specimen which was subjected to significant axial load has undergone non-uniform out-of-plane displacement (although the specimen has been constraint with roller in the out-of-plane direction) which was recorded as 1.5 mm at LVDTs 18 and 19 [13].

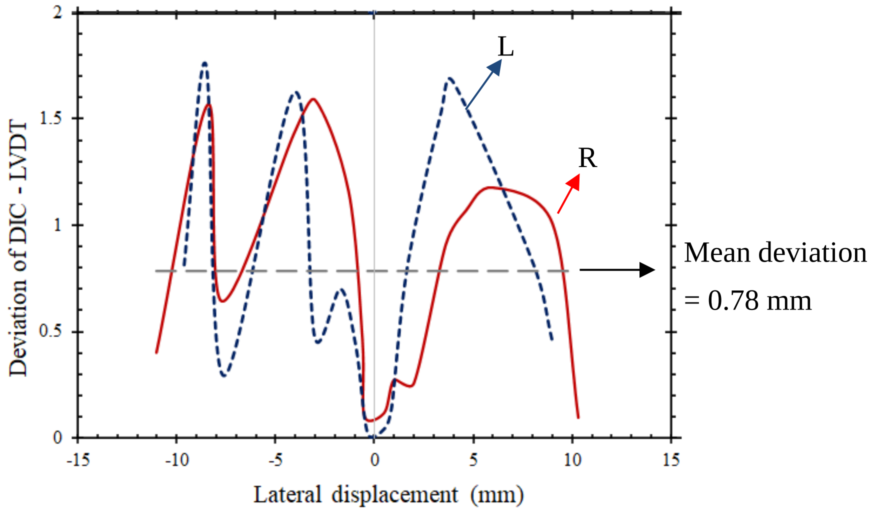

Fig. 15. Measurement deviation of DIC compared to LVDTs in RC shear wall tests under cyclic loading. (Note: L = DIC-L compared to LVDT-2 and R = DIC-R compared to LVDT-5)

4.5. Discussion of case studies

It is noted that the three case studies were selected based on the order of displacement to be measured and the nature of deformation for concrete structures. The scope is to illustrate the necessity of optimising the parameters and application of the proposed framework. Therefore, the details of experiments are focused on the experimental setting and selected parameters related to the quality of captured images and analysis accuracy. Interested readers can find out more details on the experimental setup and implementation of the case studies in the cited references 13, 15, 39 and 41.

The presented specifications of camera and lens, as well as the selected DIC parameters of the three case studies can be taken as rational estimation when applying DIC for reinforcement corrosion induced concrete crack, crack measurement of pre-notched concrete beam and seismic performance of RC shear walls. However, the camera and parameters should be examined to attain the required accuracy in accordance with any new problem.

It is acknowledged that using real images with available camera and setup is the best way to evaluate measurement accuracy. However, it is unlikely to be able to prepare the setup and samples before checking the feasibility of experimental scheme, as the fabrication of formwork and cast of samples (especially large samples as in case study 3) are expensive and time-consuming. In most cases, real images are generally unavailable at the stage of experimental design before implementation.

On the contrary, the proposed a priori analysis method (Step 4a of the framework) can estimate the theoretical accuracy for selection of camera, fabrication of speckles on samples and evaluation of the feasibility of experimental scheme. It is useful and worthy in designing for experiment to measure displacement. However, validation of accuracy analysis by using real images during implementation is still highly recommended if they are available.

5. Conclusion

A systematic framework that optimises the design of image acquisition system and different parameters in displacement measurement with 2D DIC for concrete structures at different scales is proposed and illustrated through three case studies. Based on an accuracy analysis with simulated deformation images, it is found that the standard uncertainty of strain is extremely high when a small subset size (less than 45×45 pixels) is used. The effects of subset size on the measurement accuracy of displacement and the mean error of strain are insignificant. The optimal step size is proposed to be less than half of the subset size.

The example of a subset size of 45 × 45 pixels with different mean speckle size m and speckle spacing ρ demonstrates the varying accuracy of DIC measurements for preassigned rigid displacement of 0.1 pixel and uniaxial tensile strain of 1000 με. It is observed that when $1 \leq \rho/m \leq 3$, the mean displacement and strain error, and the STD of strain generally decrease with smaller speckle size. Higher speckle density (i.e. smaller speckle spacing ρ) does not necessarily improve the accuracy of displacement and strain measurement. However, when $\rho/m \geq 3$, the STD of strain increases drastically.

The measurement deviations of DIC were presented by comparing the results with point-contact devices (i.e., clip gauge or LVDTs) and alternative non-contact method (i.e., ESPI), to show the effectiveness of the proposed optimisation framework. The proposed DIC parameters for concrete structures at different scales (and different order of accuracy), demonstrated with three examples, are foreseen to be a useful reference source for any structural engineer interested in exploring the use of 2D DIC measurements.

6. Acknowledgements

The authors appreciate the information provided by Dr. Clement Barthes, the developer of DIC software Optecal. Support from the General Research Fund of Hong Kong (HKU 17223916) is gratefully acknowledged.

References

[1] Gencturk B, Hossain K, Kapadia A, Labib E, Mo YL. Use of digital image correlation technique in full-scale testing of prestressed concrete structures. Measurement 2014; 47(1): 505-515.

[2] Peters WH, Ranson WF. Digital imaging techniques in experimental stress analysis. Opt Eng 1982; 21(3): 427–431.

[3] Corr D, Accardi M, Graham-Brady L, Shah S. Digital image correlation analysis of interfacial debonding properties and fracture behavior in concrete. Eng Fract Mech 2007; 74(1): 109-121.

[4] Destrebecq JF, Toussaint E, Ferrier E. Analysis of cracks and deformations in a full scale reinforced concrete beam using a digital image correlation technique. Exp Mech 2011; 51(6): 879-890.

[5] Lin Q, Yuan H, Biolzi L, Labuz JF. Opening and mixed mode fracture processes in a quasi-brittle material via digital imaging. Eng Fract Mech 2014; 131: 176-193.

[6] Carpiuc-Prisacari A, Poncelet M, Kazymyrenko K, Hild F, Leclerc H. Comparison between experimental and numerical results of mixed-mode crack propagation in concrete: Influence of boundary conditions choice. Cem Conc Res 2017; 100: 329-340.

[7] Gheitasi A, Harris DK, Hansen M. An experimental-computational correlated study for describing the failure characteristics of concrete across two scale levels: Mixture and structural component. Exp. Mech. 2018; 58(1): 11-32.

[8] Ghorbani R, Matta F, Sutton MA. Full-field deformation measurement and crack mapping on confined masonry walls using digital image correlation. Exp Mech 2015; 55(1): 227-243.

[9] Debasis D, Bhattacharjee S. Optical strain for monitoring of concrete failure mechanism with discontinuity. Appl Opt 2015; 54(35): 10409-10417.

[10] Leibovich O, Yankelevsky DZ, Dancygier AN. Direct digital image analysis of local displacements and strains in a pull-out test. Structures Elsevier 2018; 14: 230-242.

[11] Bompa DV, Elghazouli AY. Monotonic and cyclic performance of threaded

reinforcement splices. Structures Elsevier 2018; 16: 358-372.

[12] De Wilder K, Lava P, Debruyne D, Wang Y, De Roeck G, Vandewalle L. Stress field based truss model for shear-critical prestressed concrete beams. Structures Elsevier 2015; 3: 28-42.

[13] Looi DTW, Su RKL, Cheng B, Tsang HH. Effects of axial load on seismic performance of reinforced concrete walls with short shear span. Eng Struct 2017; 151: 312-326.

[14] Michel A, Pease BJ, Peterová A, Geiker MR, Stang H, Thybo AEA. Penetration of corrosion products and corrosion-induced cracking in reinforced cementitious materials: Experimental investigations and numerical simulations. Cem Conc Comp 2014; 47: 75-86.

[15] Liu QF, Su RKL. A displacement-based inverse analysis method to estimate in-situ Young's modulus of steel rust in reinforced concrete. Eng Fract Mech 2018; 192: 114-128.

[16] Lecompte D, Smits A, Bossuyt S, Sol H, Vantomme J, Hemelrijck DV, Habraken AM. Quality assessment of speckle patterns for digital image correlation. Opt Laser Eng 2006; 44(11): 1132–1145.

[17] Wang ZY, Li HQ, Tong JW, Ruan JT. Statistical analysis of the effect of intensity pattern noise on the displacement measurement precision of digital image correlation using self-correlated images. Exp Mech 2007; 47(5): 701–707.

[18] Chen ZN, Shao XX, Xu XY, He XY. Optimized digital speckle patterns for digital image correlation by consideration of both accuracy and efficiency. Appl Opt 2018; 57(4): 884-893.

[19] Pan B, Xie H, Wang Z, Qian K, Wang Z. Study on subset size selection in digital image correlation for speckle patterns. Opt Express 2008; 16(10): 7037-7048.

[20] Kibitkin V, Solodushkin A, Pleshanov V, Napryushkin A. On a choice of input

parameters for calculation the vector field and deformation with DIC. Measurement 2017; 95: 266-272.

[21] Triconnet K, Derrien K, Hild F, Baptiste D. Parameter choice for optimized digital image correlation. Opt Laser Eng 2009; 47(6): 728-737.

[22] Kozicki J, Tejchman J. Application of DIC technique to concrete—study on objectivity of measured surface displacements. Exp Mech 2013; 53(9): 1545-1559.

[23] Tu P, Liu X. An error criterion in digital image correlation for unknown deformation fields and its application of parameters selection. Exp Mech 2017; 57(5): 783-799.

[24] Schreier H, Orteu JJ, Sutton MA. Image correlation for shape, motion and deformation measurements: Basic concepts, theory and applications. Springer Science & Business Media; 2009.

[25] Pan B, Qian K, H. Xie H, Asundi A. Two-dimensional digital image correlation for in-plane displacement and strain measurement: a review. Meas Sci Technol 2009; 20(6): 062001.

[26] Schreier HW, Sutton MA. Systematic errors in digital image correlation due to undermatched subset shape functions. Exp Mech 2002; 42(3): 303-310.

[27] Bruck HA, McNeill SR, Sutton MA, Peters WH. Digital image correlation using Newton-Raphson method of partial differential correction. Exp Mech 1989; 29(3): 261-267.

[28] Zhou P, Goodson KE. Subpixel displacement and deformation gradient measurement using digital image/speckle correlation. Opt Eng 2001; 40(8): 1613-1620.

[29] Forsey A, Gungor S. Demosaicing images from colour cameras for digital image correlation. Opt Laser Eng 2016; 86: 20-28.

[30] Sakanashi Y, Gungor S, Bouchard PJ. Measurement of Creep Deformation in

Stainless Steel Welded Joints. In: Proceedings of the SEM Annual Conference. USA: Mohegan Sun, Uncasville, Connect; 2011, vol. 5, p. 415–422.

[31] Bouchard PJ, Sakanashi Y, Gungor S. Spatially resolved creep deformation of a thick section stainless steel welded joint. In: Proceedings of the 3rd International ECCC – Creep Fracture Conference, Rome; 2014.

[32] *Optecal DIC Software*, CV Measurements, Berkeley, CA; 2015.

[33] http://hugin.sourceforge.net/. Accessed 8 July 2020.

[34] http://www.vision.caltech.edu/bouguetj/calib_doc/. Accessed 8 July 2020.

[35] Liu QF, Su RKL. A Wasserstein distance-based analogous method to predict distribution of non-uniform corrosion on reinforcements in concrete. Constr Build Mater 2019; 226: 965-975.

[36] BS ISO 12232: Photography — Digital still cameras — Determination of exposure index, ISO speed ratings, standard output sensitivity, and recommended exposure index; 2006.

[37] Taylor BN, Guidelines for evaluating and expressing the uncertainty of NIST measurement results (rev.). DIANE; 2009.

[38] Sun YF, Pang JHL. Study of optimal subset size in digital image correlation of speckle pattern images. Opt Laser Eng 2007; 45(9): 967-974.

[39] Chen HH, Su RKL. Tension softening curves of plain concrete. Constr Build Mater 2013; 44: 440-451.

[40] Manning JM, Lee CK, Cerami A. Draft recommendation: Determination of the fracture energy of mortar and concrete by means of three-point bend tests on notched beams. Mater Struct 1985; 18: 484.

[41] Su RKL, Chen HH, Fok SL, Li H, Singh G, Sun L, Shi L. Determination of the tension softening curve of nuclear graphites using the incremental displacement collocation method. Carbon 2013; 57: 65–78.

[42] Chen HH, Su RKL. Correction of strain errors induced by small rigid-body motions in electronic speckle pattern interferometry measurement. HKIE Trans 2013; 20: 2-11.

[43] Brillaud J, Fabienne L. Limits and possibilities of laser speckle and white-light image-correlation methods: theory and experiments. Appl Opt 2002; 41(31): 6603-6613.